Springer

Acta Mechanica Sinica

CrossMark click for updates

• RESEARCH PAPER •

Acta Mech. Sin., Vol. 41, 124342 (2025)
https://doi.org/10.1007/s10409-024-24342-x

A multiscale analytical model for superelastic deformation of gradient nano-grained NiTi shape memory alloys

Bo Xu[1], Xingyu Zhou[2], and Chao Yu[2*]

[1] *Failure Mechanics and Engineering Disaster Prevention, Key Laboratory of Sichuan Province, Sichuan University, Chengdu 610065, China;*
[2] *Applied Mechanics and Structure Safety Key Laboratory of Sichuan Province, School of Mechanics and Aerospace Engineering, Southwest Jiaotong University, Chengdu 610031, China*

Received June 3, 2024; accepted September 10, 2024; published online December 18, 2024

A multiscale nonlocal continuum model is proposed to describe the superelastic deformation of gradient nano-grained NiTi shape memory alloys (SMAs). At the mesoscopic scale, the polycrystalline aggregate is regarded as a composite, i.e., the grain-interior (GI) phase is assumed to be a cuboidal inclusion embedded in a matrix of grain-boundary (GB) phase. An intrinsic energetic length and a gradient energy are introduced into the Helmholtz free energy of the GI phase. The criterion of martensite transformation (MT) is derived based on the principle of virtual power and second law of thermodynamics. The hindering effect of GB on MT in GI phase is addressed. By deriving the analytical solution of the proposed model and introducing a scale transition rule, the overall and local stress-strain responses of the specimen at the macroscopic scale are obtained. The prediction capability of the proposed model is verified by comparing the analytical solution with the experiment. The influences of the distribution form for the grain size (GS) on the superelastic deformation of gradient nano-grained NiTi SMAs are further predicted and discussed. The analytical form and low computational cost of the proposed model make it an appropriate theoretical tool to design the gradient nano-grained SMAs with desired mechanical property.

Gradient nano-grained NiTi SMA, Multiscale continuum model, Analytical solution, Martensite transformation, Superelasticity

Citation: B. Xu, X. Zhou, and C. Yu, A multiscale analytical model for superelastic deformation of gradient nano-grained NiTi shape memory alloys, Acta Mech. Sin. 41, 124342 (2025), https://doi.org/10.1007/s10409-024-24342-x

1. Introduction

Shape memory alloys (SMAs) exhibit unique superelasticity and shape memory effect, and have been successfully utilized as core-component materials in various engineering fields such as aerospace, biomedical, mechanical engineering, and microelectromechanical systems [1]. The diverse engineering applications of SMA structures and devices pose distinct requirements on their service performances. For instance, in the field of solid-state refrigeration, it is expected that SMAs can exhibit significant isothermal entropy change or adiabatic temperature change during martensite transformation (MT) [2-4]. As a seismic damper, SMAs with large stress-strain hysteresis loop are needed to ensure the sufficient energy absorption capacity [5,6]. As an actuator, SMAs should exhibit obvious transformation hardening and small strain-temperature hysteresis loop to achieve the accurate driving control [7-10]. Moreover, in long time service, the cyclic stability of SMAs is an important evaluation indicator [11-13]. Since these service performances at the macroscopic scale are determined by the microstructure characteristics, the mechanical properties of SMAs can be tailored by changing the grain size (GS).

Grain refinement has been commonly employed in conventional metallic materials as a means to enhance the strength of material. As the GS decreases, conventional metallic materials can exhibit higher yield strength, which is often inversely proportional to the square root of the GS, i.e., the well-known Hall-Petch relation [14,15]. GS also

*Correspondent author. E-mail address: chaoyu@home.swjtu.edu.cn (Chao Yu)
Executive Editor: Wei Hong

significantly influences the stress-induced MT in SMAs. Through a severe plastic deformation process such as cold rolling or cold drawing, as well as subsequent annealing, the GS of NiTi SMA can be reduced to the nanometer scale (< 100 nm). Due to the strong effect of GS on the MT when the GS < ~80 nm, as the GS decreases, the superelastic stress-strain curve of NiTi SMAs changes from the "plateau-type" to a "hardening-type", with an increase in transformation hardening modulus and a significant reduction in dissipation energy [16-19]. The GS-dependent superelasticity of NiTi SMAs has been widely investigated in the last decade [10-12,20-29].

Gradient-grained metals and alloys have manifested themselves with excellent mechanical properties as compared to their homogeneous counterparts, which have attracted much attention [30]. Interestingly, due to the GS dependence of MT in SMAs, the gradient nano-grained SMAs can show unprecedented mechanical and functional properties [31-35]. Huang et al. [31] fabricated the gradient nano-grained NiTi SMA sheet with the GS ranging from 25 to 175 nm along the axial direction in an approximately linear distribution. The quasi-static loading experiments indicated that, compared to the specimens with uniform GS, the superelasticity of gradient nano-grained NiTi SMA exhibited a wider range of response stress. Chen et al. [32] prepared a series of uniformly fine-grained, uniformly nano-grained and gradient nano-grained NiTi SMA sheets, and further investigated the rate-dependent superelastic deformation of these materials. Experimental results showed that the transformation hardening modulus of coarse-grained specimen increased with the strain rate due to the strong thermomechanical coupling effect. However, such rate dependence is significantly weakened in nano-grained specimen owing to the weaker temperature variation together with the weaker transformation temperature dependence. Meanwhile, the rate dependence of superelasticity in the gradient nano-grained specimens fell between those of fine-grained and nanocrystalline ones. Recently, Chen et al. [13,33,34,36] prepared the NiTi SMA plates with the GS gradients in the thickness and width directions, which showcased superior elastocaloric effect and cyclic stability, compared to the coarse-grained NiTi SMAs. So far, it has been revealed that the mechanical properties of NiTi SMAs can be significantly improved by introducing the gradient nano-grained microstructures.

To assess the service performance of SMA devices, it is essential to establish appropriate theoretical models. In the last decades, significant efforts have been devoted to developing the continuum models of SMAs. Comprehensive reviews of this topic can be found in Refs. [37-39], and recent representative works can be referred to Refs. [40-58], and so on. However, few works incorporated the GS effect. Sun and He [59] constructed a multiscale continuum model and successfully described the dependence of energy dissipation on the GS. Li and Sun [60] developed a one-dimensional (1D) core-shell model for nanocrystalline SMAs. The predicted results showed that with the reduction of GS, the energy of grain-boundary (GB) phase gradually became dominant during MT, and brought a fundamental change in the growth mode of martensite. Qiao and Radovitzky [61] and Qiao et al. [62] constructed 1D and three-dimensional (3D) non-local models by introducing two intrinsic length scales. The increased transformation hardening modulus with the decrease of GS and specimen size was well captured. Meanwhile, a 3D constitutive model based on micromechanics was also developed, and reasonably captured the GS-dependent stress-strain responses of SMAs [63]. However, the aforementioned models are only applicable for SMAs with uniformly distributed GS. Although few phase field models have been developed in recent years for the gradient nano-grained SMAs and revealed the synergic deformation mechanism of the coarse-grain and nano-grain [64,65], it was difficult to reflect the real gradient microstructure in the materials due to the huge computational cost for such type of model. As a result, the experimental stress-strain responses of the gradient nano-grained NiTi SMAs cannot be accurately reproduced.

In this work, we will develop a multiscale nonlocal continuum model aimed at describing the superelastic deformation of gradient nano-grained NiTi SMAs and providing a theoretical tool to design this type of material with desired mechanical property. At the mesoscopic scale, the polycrystalline aggregate is regarded as a composite, i.e., the grain-interior (GI) phase is assumed to be a cuboidal inclusion embedded in a matrix of GB phase. An intrinsic energetic length and a gradient energy are introduced into the Helmholtz free energy of the GI phase. The criterion of MT is derived based on the principle of virtual power and second law of thermodynamics, and the hindering effect of GB on MT in GI phase is addressed. By deriving the analytical solution of the proposed model and introducing a scale transition rule, the overall and local stress-strain responses of the specimen at the macroscopic scale are obtained. The prediction capability of the proposed model is verified by comparing the analytical solution with the experiments.

2. Multiscale nonlocal continuum model

The gradient nano-grained NiTi SMA specimen can be prepared by gradient heat treatment after severe plastic deformation [32]. As shown in Fig. 1(a), the average GS varies from a few nanometers at one end of the specimen to one hundred or even a few ten hundred nanometers at the other end along the axial direction. Thus, at the macroscopic scale,

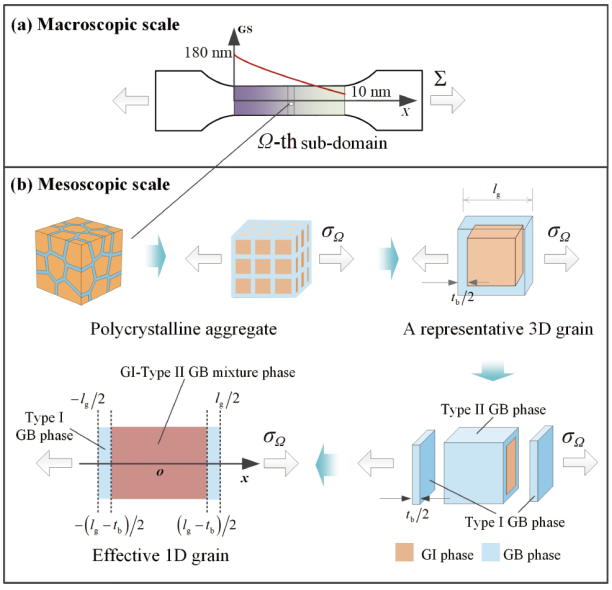

Figure 1 Schematic of the multiscale model. (a) The gradient nano-grained NiTi SMA specimen at the macroscopic scale; (b) polycrystalline aggregate, a representative 3D grain and the simplified effective 1D grain at the mesoscopic scale.

we can divide the specimen into a series of sub-domains with an identical length, i.e., $l_\Omega = l/N$, where l is the gauge length of the specimen, N is the total number of the sub-domains, l_Ω denotes the length of the Ω-th sub-domain. The GS in a given sub-domain can be regarded as uniform if N is large enough. In a smaller spatial scale (mesoscopic scale), the microstructure of a sub-domain emerges. It means that a sub-domain in the macroscopic scale becomes a polycrystalline aggregate containing a large number of grains at the mesoscopic scale. From a modelling point of view, the polycrystalline aggregate can be described as a core-shell type "GI-GB composite", i.e., the GI phase is assumed to be a cuboidal inclusion embedded in a matrix of GB phase, as shown in Fig. 1(b) (this approach was also adopted in Refs. [60,62]). However, in order to obtain the analytical solution of the proposed model, further simplification is necessary. Firstly, the polycrystalline aggregate can be regarded as the repeated arrangement of the grains in the space. Thus, the deformation response of the polycrystalline aggregate can be replaced by a representative grain. Secondly, generally speaking, the strain field along the axial direction in such a grain is 3D. However, when the grain is subjected to a uniaxial mechanical loading as shown in Fig. 1(b), inspired by the work of Li and Sun [60], we can assume that the axial strain is uniformly distributed in the square cross section perpendicular to the axial direction, i.e., $\varepsilon = \varepsilon(x)$ (to avoid confusion, the spatial coordinates at the macroscopic and mesoscopic scales are denoted as X and x, respectively). In this case, the 3D grain is reduced into an effective 1D grain (see Fig. 1(b)). Such 3D→1D effective modelling is expected to retain the key features of the 3D polycrystalline aggregate such as the volume fraction of GB and its deformation constraint to the GI phase.

Consider an effective 1D grain in the Ω-th sub-domain of the specimen. The local stress applied on this sub-domain is denoted as σ_Ω. The volume fraction of the GB phase can be calculated as $f_{\mathrm{GB},\Omega} = 1-\left(1-t_\mathrm{b}/l_{\mathrm{g},\Omega}\right)^3$, where $l_{\mathrm{g},\Omega}$ represents the grain size of the Ω-th sub-domain, t_b is the thickness of GB, which is a constant. According to the geometric and deformation features of the 1D grain, we further divide the GB phase into two categories, the type I GB and type II GB, as shown in Fig. 1(b). For a point x at the mesoscopic scale, when $-l_{\mathrm{g},\Omega}/2 \leqslant x < -\left(l_{\mathrm{g},\Omega}-t_\mathrm{b}\right)/2$ or $\left(l_{\mathrm{g},\Omega}-t_\mathrm{b}\right)/2 < x \leqslant l_{\mathrm{g},\Omega}/2$, it belongs to the type I GB phase; when $-\left(l_{\mathrm{g},\Omega}-t_\mathrm{b}\right)/2 \leqslant x \leqslant \left(l_{\mathrm{g},\Omega}-t_\mathrm{b}\right)/2$, it belongs to the GI-type II GB mixture phase. The volume fractions of these two GB phases can be, respectively, calculated as $f_{\mathrm{GB_I},\Omega} = t_\mathrm{b}/l_{\mathrm{g},\Omega}$ and $f_{\mathrm{GB_{II}},\Omega} = \left(1-t_\mathrm{b}/l_{\mathrm{g},\Omega}\right)\left(2-t_\mathrm{b}/l_{\mathrm{g},\Omega}\right)t_\mathrm{b}/l_{\mathrm{g},\Omega}$. The Helmholtz free energies of type I GB ($\psi_{\mathrm{GB_I},\Omega}$), type II GB ($\psi_{\mathrm{GB_{II}},\Omega}$) and GI ($\psi_{\mathrm{GI},\Omega}$) phases can be formulated as

$$\psi_{\mathrm{GB_I},\Omega}(x) = \frac{1}{2}E_\mathrm{GB}\left[\varepsilon_\Omega(x)\right]^2,$$
$$x \in \left[-\frac{l_{\mathrm{g},\Omega}}{2}, -\frac{l_{\mathrm{g},\Omega}-t_\mathrm{b}}{2}\right] \cup \left[\frac{l_{\mathrm{g},\Omega}-t_\mathrm{b}}{2}, \frac{l_{\mathrm{g},\Omega}}{2}\right], \tag{1a}$$

$$\psi_{\mathrm{GB_{II}},\Omega}(x) = \frac{1}{2}E_\mathrm{GB}\left[\varepsilon_\Omega(x)\right]^2,$$
$$x \in \left[-\frac{l_{\mathrm{g},\Omega}-t_\mathrm{b}}{2}, \frac{l_{\mathrm{g},\Omega}-t_\mathrm{b}}{2}\right], \tag{1b}$$

$$\psi_{\mathrm{GI},\Omega}(x) = \frac{1}{2}E_\mathrm{GI}\left[\varepsilon_\Omega(x)-\varepsilon_\Omega^{\mathrm{tr}}(x)\right]^2 + \Delta s_\mathrm{GI}^{\theta_0}(\theta-\theta_0)\xi_\Omega(x) + \frac{1}{2}S_0 l_\mathrm{e}^2\left(\xi_{\Omega,x}\right)^2,$$
$$x \in \left[-\frac{l_{\mathrm{g},\Omega}-t_\mathrm{b}}{2}, \frac{l_{\mathrm{g},\Omega}-t_\mathrm{b}}{2}\right], \tag{1c}$$

where E_GB and E_GI represent the elastic moduli of GB and GI phases, respectively. $\varepsilon_\Omega(x)$ represents the total strain at point x. $\varepsilon_\Omega^{\mathrm{tr}}(x)$ and $\xi_\Omega(x)$ are the transformation strain and the volume fraction of martensite phase at point x in the GI phase (noted that $0 \leqslant \xi_\Omega(x) \leqslant 1$), and there is a linear relationship between $\varepsilon_\Omega^{\mathrm{tr}}(x)$ and $\xi_\Omega(x)$, i.e., $\varepsilon_\Omega^{\mathrm{tr}}(x) = g^{\mathrm{tr}}\xi_\Omega(x)$, g^{tr} is maximum transformation strain. $\Delta s_\mathrm{GI}^{\theta_0}$ is the entropy difference between austenite and martensite phases. θ_0 is the balance temperature. l_e is the intrinsic energetic length. S_0 is a parameter with the dimension of stress. It should be pointed out that in the GI phase, both the elastic and transformation strains are taken into account, i.e.,

$\varepsilon_{\Omega}(x)=\varepsilon_{\Omega}^{\mathrm{e}}(x)+\varepsilon_{\Omega}^{\mathrm{tr}}(x)$, and the term $\varepsilon_{\Omega}(x)-\varepsilon_{\Omega}^{\mathrm{tr}}(x)$ in Eq. (1c) represents the elastic strain. However, owing to the non-transformable feature of GB, such a phase is modelled as a linear elastic body.

By Eqs. (1b) and (1c), the Helmholtz free energy of the GI-type II GB mixture phase can be formulated as the mixture rule

$$\begin{aligned}\psi_{\mathrm{mix},\Omega}(x)&=\frac{1-f_{\mathrm{GB_I},\Omega}-f_{\mathrm{GB_{II}},\Omega}}{1-f_{\mathrm{GB_I},\Omega}}\psi_{\mathrm{GI},\Omega}(x)+\frac{f_{\mathrm{GB_{II}},\Omega}}{1-f_{\mathrm{GB_I},\Omega}}\psi_{\mathrm{GB_{II}},\Omega}(x)\\&=\frac{1}{2}E_{\mathrm{GI\text{-}GB},\Omega}\left[\varepsilon_{\Omega}(x)-\bar{\varepsilon}_{\Omega}^{\mathrm{tr}}(x)\right]^2+\Delta\bar{s}_{\Omega}^{\theta_0}(\theta-\theta_0)\xi_{\Omega}(x)\\&\quad+\frac{1}{2}A_{\Omega}\xi_{\Omega}^2(x)+\frac{1}{2}B\left(\xi_{\Omega,x}\right)^2,\end{aligned}\tag{2}$$

where

$$E_{\mathrm{GI\text{-}GB},\Omega}=\left(\frac{f_{\mathrm{GB_{II}},\Omega}}{1-f_{\mathrm{GB_I},\Omega}}\right)E_{\mathrm{GB}}+\left(\frac{1-f_{\mathrm{GB_I},\Omega}-f_{\mathrm{GB_{II}},\Omega}}{1-f_{\mathrm{GB_I},\Omega}}\right)E_{\mathrm{GI},\Omega},\tag{3a}$$

$$\bar{\varepsilon}_{\Omega}^{\mathrm{tr}}(x)=g^{\mathrm{tr}}\left(\frac{1-f_{\mathrm{GB_I},\Omega}-f_{\mathrm{GB_{II}},\Omega}}{1-f_{\mathrm{GB_I},\Omega}}\right)\left(\frac{E_{\mathrm{GI}}}{E_{\mathrm{GI\text{-}GB},\Omega}}\right)\xi_{\Omega}(x),\tag{3b}$$

$$\Delta\bar{s}_{\Omega}^{\theta_0}=\left(\frac{1-f_{\mathrm{GB_I},\Omega}-f_{\mathrm{GB_{II}},\Omega}}{1-f_{\mathrm{GB_I},\Omega}}\right)\Delta s_{\mathrm{GI}}^{\theta_0},\tag{3c}$$

$$\begin{aligned}A_{\Omega}=E_{\mathrm{GI\text{-}GB},\Omega}(g^{\mathrm{tr}})^2&\left(\frac{1-f_{\mathrm{GB_I},\Omega}-f_{\mathrm{GB_{II}},\Omega}}{1-f_{\mathrm{GB_I},\Omega}}\right)\left(\frac{E_{\mathrm{GI}}}{E_{\mathrm{GI\text{-}GB},\Omega}}\right)\\&\cdot\left[1-\left(\frac{1-f_{\mathrm{GB_I},\Omega}-f_{\mathrm{GB_{II}},\Omega}}{1-f_{\mathrm{GB_I},\Omega}}\right)\left(\frac{E_{\mathrm{GI}}}{E_{\mathrm{GI\text{-}GB},\Omega}}\right)\right],\end{aligned}\tag{3d}$$

$$B_{\Omega}=\left(\frac{1-f_{\mathrm{GB_I},\Omega}-f_{\mathrm{GB_{II}},\Omega}}{1-f_{\mathrm{GB_I},\Omega}}\right)S_0 l_{\mathrm{e}}^2.\tag{3e}$$

$E_{\mathrm{GI\text{-}GB},\Omega}$, $\bar{\varepsilon}_{\Omega}^{\mathrm{tr}}(x)$ and $\Delta\bar{s}_{\Omega}^{\theta_0}$ are the effective elastic modulus, transformation strain and entropy difference between austenite and martensite of the GI-type II GB mixture phase, respectively. Noted that A_{Ω} and B_{Ω} are always positive. The hindering effect of GB on the MT in GI phase is partly reflected by Eqs. (3b) and (3d). On one hand, it can be easily proven that $\bar{\varepsilon}_{\Omega}^{\mathrm{tr}}(x)$ is a monotonic decreasing function of $f_{\mathrm{GB_{II}},\Omega}$, which means the maximum transformation strain in the GI-type II GB mixture phase decreases with increasing the volume fraction of type II GB phase; on the other hand, the term $\frac{1}{2}A_{\Omega}\xi^2(x)$ in Eq. (2) represents an additional transformation hardening energy, which is also governed by $f_{\mathrm{GB_{II}},\Omega}$.

Considering any segment of the GI-type II GB mixture phase $x\in[x_1,x_2]\,\big|\,-\frac{l_{\mathrm{g},\Omega}-t_{\mathrm{b}}}{2}\leqslant x\leqslant\frac{l_{\mathrm{g},\Omega}-t_{\mathrm{b}}}{2}$, the internal power in this segment can be defined as [62,66]

$$P_{\Omega}^{\mathrm{int}}\left(\dot{\varepsilon}_{\Omega},\dot{\bar{\varepsilon}}_{\Omega}^{\mathrm{tr}},\dot{\xi}_{\Omega}\right)=\int_{x_1}^{x_2}\left[\sigma_{\Omega}\left(\dot{\varepsilon}_{\Omega}-\dot{\bar{\varepsilon}}_{\Omega}^{\mathrm{tr}}\right)+k_{\Omega}\dot{\xi}_{\Omega}+w_{\Omega}\dot{\xi}_{\Omega,x}\right]\mathrm{d}x,\tag{4}$$

where k_{Ω} and w_{Ω} are the work conjugates to the martensite volume fraction ξ_{Ω} and its gradient $\xi_{\Omega,x}$, respectively. The external power expended on this segment can be formulated as

$$P_{\Omega}^{\mathrm{ext}}\left(\dot{u}_{\Omega},\dot{\xi}_{\Omega}\right)=\left(\hat{t}_{\Omega}\dot{u}_{\Omega}+\hat{k}_{\Omega}\dot{\xi}_{\Omega}\right)\Big|_{x_1}^{x_2},\tag{5}$$

where $\hat{t}_{\Omega}$ is the applied boundary traction, $\hat{k}_{\Omega}$ is work conjugate to the martensite volume fraction ξ_{Ω} at the boundary, u_{Ω} is the displacement. We further introduce the principle of virtual power, i.e.,

$$P_{\Omega}^{\mathrm{int}}\left(\dot{\tilde{\varepsilon}}_{\Omega},\dot{\tilde{\bar{\varepsilon}}}_{\Omega}^{\mathrm{tr}},\dot{\tilde{\xi}}_{\Omega}\right)=P_{\Omega}^{\mathrm{ext}}\left(\dot{\tilde{u}}_{\Omega},\dot{\tilde{\xi}}_{\Omega}\right),\tag{6}$$

where $\tilde{u}_{\Omega}$, $\tilde{\varepsilon}_{\Omega}$, $\tilde{\bar{\varepsilon}}_{\Omega}^{\mathrm{tr}}$ and $\tilde{\xi}_{\Omega}$ are the virtual displacement, strain, transformation strain and martensite volume fraction, respectively, and they satisfy the constraint of deformation compatibility, i.e., $\tilde{u}_{\Omega,x}=\tilde{\varepsilon}_{\Omega}-\tilde{\bar{\varepsilon}}_{\Omega}^{\mathrm{tr}}+\bar{g}_{\Omega}^{\mathrm{tr}}\tilde{\xi}_{\Omega}$ (where $\bar{g}_{\Omega}^{\mathrm{tr}}$ represents the effective maximum transformation strain, according to Eq. (3b), we have $\bar{g}_{\Omega}^{\mathrm{tr}}=g^{\mathrm{tr}}\left(\frac{1-f_{\mathrm{GB_I},\Omega}-f_{\mathrm{GB_{II}},\Omega}}{1-f_{\mathrm{GB_I},\Omega}}\right)\cdot\left(\frac{E_{\mathrm{GI}}}{E_{\mathrm{GI\text{-}GB},\Omega}}\right)$). Substituting Eqs. (4) and (5) into Eq. (6), it yields

$$\begin{aligned}&P_{\Omega}^{\mathrm{int}}\left(\dot{\tilde{\varepsilon}}_{\Omega},\dot{\tilde{\bar{\varepsilon}}}_{\Omega}^{\mathrm{tr}},\dot{\tilde{\xi}}_{\Omega}\right)-P_{\Omega}^{\mathrm{ext}}\left(\dot{\tilde{u}}_{\Omega},\dot{\tilde{\xi}}_{\Omega}\right)\\&=\int_{x_1}^{x_2}\left[\sigma_{\Omega}\left(\dot{\tilde{\varepsilon}}_{\Omega}-\dot{\tilde{\bar{\varepsilon}}}_{\Omega}^{\mathrm{tr}}\right)+k_{\Omega}\dot{\tilde{\xi}}_{\Omega}+w_{\Omega}\dot{\tilde{\xi}}_{\Omega,x}\right]\mathrm{d}x-\left(\hat{t}_{\Omega}\dot{\tilde{u}}_{\Omega}+\hat{k}_{\Omega}\dot{\tilde{\xi}}_{\Omega}\right)\Big|_{x_1}^{x_2}\\&=\int_{x_1}^{x_2}\sigma_{\Omega,x}\dot{\tilde{u}}_{\Omega}\mathrm{d}x+\int_{x_1}^{x_2}\left(k_{\Omega}-\bar{g}_{\Omega}^{\mathrm{tr}}\sigma_{\Omega}-w_{\Omega,x}\right)\dot{\tilde{\xi}}_{\Omega}\mathrm{d}x+\left(\sigma_{\Omega}-\hat{t}_{\Omega}\right)\dot{\tilde{u}}_{\Omega}\Big|_{x_1}^{x_2}\\&\quad+\left(w_{\Omega}-\hat{k}_{\Omega}\right)\dot{\tilde{\xi}}_{\Omega}\Big|_{x_1}^{x_2}\\&=0.\end{aligned}\tag{7}$$

Since Eq. (7) should be always satisfied for any integral interval $[x_1,x_2]$, it requires

$$\sigma_{\Omega,x}=0,\tag{8a}$$

$$k_{\Omega}-\bar{g}_{\Omega}^{\mathrm{tr}}\sigma_{\Omega}-w_{\Omega,x}=0,\tag{8b}$$

$$\hat{t}_{\Omega}(x_1)=\sigma_{\Omega}(x_1),\ \hat{t}_{\Omega}(x_2)=\sigma_{\Omega}(x_2),\tag{8c}$$

$$\hat{k}_{\Omega}(x_1)=w_{\Omega}(x_1),\ \hat{k}_{\Omega}(x_2)=w_{\Omega}(x_2).\tag{8d}$$

Eqs. (8a) and (8b) are the force and micro-force balance equations, Eqs. (8c) and (8d) represent the boundary conditions. Considering the second law of thermodynamics

$$\dot{\Gamma}_{\Omega}=P_{\Omega}^{\mathrm{ext}}\left(\dot{u}_{\Omega},\dot{\xi}_{\Omega}\right)-\frac{\mathrm{d}}{\mathrm{d}t}\left[\int_{x_1}^{x_2}\psi_{\mathrm{mix},\Omega}(x)\mathrm{d}x\right]\geqslant 0,\tag{9}$$

where $\dot{\Gamma}_{\Omega}$ is the rate of energy dissipation. Substituting Eqs. (2) and (5) into Eq. (9), we can obtain

$$\dot{\Gamma}_{\Omega}=\left(\sigma_{\Omega}-\frac{\partial\psi_{\mathrm{mix},\Omega}}{\partial\varepsilon_{\Omega}^{\mathrm{e}}}\right)\dot{\varepsilon}_{\Omega}^{\mathrm{e}}+\left(k_{\Omega}-\frac{\partial\psi_{\mathrm{mix},\Omega}}{\partial\xi_{\Omega}}\right)\dot{\xi}_{\Omega}+\left(w_{\Omega}-\frac{\partial\psi_{\mathrm{mix},\Omega}}{\partial\xi_{\Omega,x}}\right)\dot{\xi}_{\Omega,x}\geqslant 0, \tag{10}$$

where $\varepsilon_{\Omega}^{\mathrm{e}}=\varepsilon_{\Omega}-\bar{\varepsilon}_{\Omega}^{\mathrm{tr}}$ is the elastic strain of GI-type II GB mixture phase. Since there is no energy dissipation in the process of elastic deformation, we have

$$\left(\sigma_{\Omega}-\frac{\partial\psi_{\mathrm{mix},\Omega}}{\partial\varepsilon_{\Omega}^{\mathrm{e}}}\right)\dot{\varepsilon}_{\Omega}^{\mathrm{e}}=0. \tag{11}$$

Owing to the arbitrariness of $\dot{\varepsilon}_{\Omega}^{\mathrm{e}}$, to satisfy Eq. (11), it requires

$$\sigma_{\Omega}=\frac{\partial\psi_{\mathrm{mix},\Omega}}{\partial\varepsilon_{\Omega}^{\mathrm{e}}}=E_{\mathrm{GI\text{-}GB},\Omega}\varepsilon_{\Omega}^{\mathrm{e}}(x)=E_{\mathrm{GI\text{-}GB},\Omega}\left[\varepsilon_{\Omega}(x)-\bar{\varepsilon}_{\Omega}^{\mathrm{tr}}(x)\right]. \tag{12}$$

Equation (12) gives the relationship between the stress and elastic strain of GI-type II GB mixture phase. As a result, Eq. (10) is reduced as

$$\dot{\Gamma}_{\Omega}=\left(k_{\Omega}-\frac{\partial\psi_{\mathrm{mix},\Omega}}{\partial\xi_{\Omega}}\right)\dot{\xi}_{\Omega}+\left(w_{\Omega}-\frac{\partial\psi_{\mathrm{mix},\Omega}}{\partial\xi_{\Omega,x}}\right)\dot{\xi}_{\Omega,x}\geqslant 0. \tag{13}$$

To satisfy Eq. (13), it is assumed that

$$k_{\Omega}=\frac{\partial\psi_{\mathrm{mix},\Omega}}{\partial\xi_{\Omega}}+Y\,\mathrm{sign}\left(\dot{\xi}_{\Omega}\right)=\Delta\bar{s}_{\Omega}^{\theta_0}(\theta-\theta_0)+A_{\Omega}\xi_{\Omega}(x)+Y\,\mathrm{sign}\left(\dot{\xi}_{\Omega}\right), \tag{14a}$$

$$w_{\Omega}=\frac{\partial\psi_{\mathrm{mix},\Omega}}{\partial\xi_{\Omega,x}}=B_{\Omega}\xi_{\Omega,x}, \tag{14b}$$

where Y is a positive constant, which represents the energy dissipation of MT and controls the width of the hysteresis loop in stress-strain response, sign(·) is the sign function. By Eqs. (14a) and (14b), it is seen that when $\dot{\xi}_{\Omega}=0$, $\dot{\Gamma}_{\Omega}=0$; when $\dot{\xi}_{\Omega}\neq 0$, $\dot{\Gamma}_{\Omega}=Y\left|\dot{\xi}_{\Omega}\right|>0$. Thus, the second law of thermodynamics can be always satisfied. Combining Eqs. (14a), (14b) and (8b), the criterion of MT can be obtained

$$\bar{g}_{\Omega}^{\mathrm{tr}}\sigma_{\Omega}-\Delta\bar{s}_{\Omega}^{\theta_0}(\theta-\theta_0)-A_{\Omega}\xi_{\Omega}(x)+B_{\Omega}\xi_{\Omega,xx}-Y\,\mathrm{sign}\left(\dot{\xi}_{\Omega}\right)=0. \tag{15}$$

For simplification, let

$$F_{\Omega}=\bar{g}_{\Omega}^{\mathrm{tr}}\sigma_{\Omega}-\Delta\bar{s}_{\Omega}^{\theta_0}(\theta-\theta_0)-Y\,\mathrm{sign}\left(\dot{\xi}_{\Omega}\right). \tag{16}$$

In the process of MT ($\dot{\xi}_{\Omega}\neq 0$), considering the boundary conditions: $\xi_{\Omega}\left(x=-\frac{l_{\mathrm{g},\Omega}-t_{\mathrm{b}}}{2}\right)=0$ and $\xi_{\Omega}\left(x=\frac{l_{\mathrm{g},\Omega}-t_{\mathrm{b}}}{2}\right)=0$ (such boundary conditions are adopted to reflect that two ends of the GI-type II GB mixture phase are obstacles to MT), the analytical solution of Eq. (15) can be formulated as

$$\xi_{\Omega}(x)=\frac{F_{\Omega}}{A_{\Omega}}\left[1-\frac{\cosh\sqrt{\frac{A_{\Omega}}{B_{\Omega}}}x}{\cosh\left(\sqrt{\frac{A_{\Omega}}{B_{\Omega}}}\frac{l_{\mathrm{g},\Omega}-t_{\mathrm{b}}}{2}\right)}\right]. \tag{17}$$

Equation (17) gives the distribution of $\xi_{\Omega}(x)$, and the maximum value of $\xi_{\Omega}(x)$ occurs at the point $x=0$. Noted that $\xi_{\Omega}(x)$ is always non-negative. Thus, when $F_{\Omega}<0$, $\xi_{\Omega}(x)$ should equal zero. Moreover, $\xi_{\Omega}(x)$ must be less than or equal to one, i.e., $\xi_{\Omega}(x)\leqslant 1$. Thus, Eq. (17) is only applicable when the maximum value of $\xi_{\Omega}(x=0)\leqslant 1$, that is

$$\xi_{\Omega,\max}=\xi_{\Omega}(0)=\frac{F_{\Omega}}{A_{\Omega}}\left[1-\frac{1}{\cosh\left(\sqrt{\frac{A_{\Omega}}{B_{\Omega}}}\frac{l_{\mathrm{g},\Omega}-t_{\mathrm{b}}}{2}\right)}\right]=1. \tag{18}$$

By Eq. (18), the critical value of F_{Ω} is determined

$$F_{\mathrm{c},\Omega}=\frac{A_{\Omega}\cosh\left(\sqrt{\frac{A_{\Omega}}{B_{\Omega}}}\frac{l_{\mathrm{g},\Omega}-t_{\mathrm{b}}}{2}\right)}{\cosh\left(\sqrt{\frac{A_{\Omega}}{B_{\Omega}}}\frac{l_{\mathrm{g},\Omega}-t_{\mathrm{b}}}{2}\right)-1}. \tag{19}$$

When $F_{\mathrm{c}}\leqslant F_{\mathrm{c},\Omega}$, the distribution of $\xi_{\Omega}(x)$ can be fully described by Eq. (17). However, when $F_{\mathrm{c}}>F_{\mathrm{c},\Omega}$, Eq. (17) is not applicable. In this case, there are two real roots for the equation $\xi_{\Omega}(x)=1$, which can be expressed as

$$x_{1,\Omega}^{*}=-\sqrt{\frac{B_{\Omega}}{A_{\Omega}}}\ln\left[\left(1-\frac{A_{\Omega}}{F_{\Omega}}\right)\cosh\left(\sqrt{\frac{A_{\Omega}}{B_{\Omega}}}\frac{l_{\mathrm{g},\Omega}-t_{\mathrm{b}}}{2}\right)+\sqrt{\left(1-\frac{A_{\Omega}}{F_{\Omega}}\right)^{2}\cosh^{2}\left(\sqrt{\frac{A_{\Omega}}{B_{\Omega}}}\frac{l_{\mathrm{g},\Omega}-t_{\mathrm{b}}}{2}\right)-1}\right], \tag{20a}$$

$$x_{2,\Omega}^{*}=\sqrt{\frac{B_{\Omega}}{A_{\Omega}}}\ln\left[\left(1-\frac{A_{\Omega}}{F_{\Omega}}\right)\cosh\left(\sqrt{\frac{A_{\Omega}}{B_{\Omega}}}\frac{l_{\mathrm{g},\Omega}-t_{\mathrm{b}}}{2}\right)+\sqrt{\left(1-\frac{A_{\Omega}}{F_{\Omega}}\right)^{2}\cosh^{2}\left(\sqrt{\frac{A_{\Omega}}{B_{\Omega}}}\frac{l_{\mathrm{g},\Omega}-t_{\mathrm{b}}}{2}\right)-1}\right]. \tag{20b}$$

As a result, in the regions $-\frac{l_{\mathrm{g},\Omega}-t_{\mathrm{b}}}{2}\leqslant x<x_{1,\Omega}^{*}$ and $x_{2,\Omega}^{*}<x\leqslant\frac{l_{\mathrm{g},\Omega}-t_{\mathrm{b}}}{2}$, the distribution of $\xi_{\Omega}(x)$ can also be described by Eq. (17); in the region $x_{1,\Omega}^{*}\leqslant x\leqslant x_{2,\Omega}^{*}$, $\xi_{\Omega}(x)=1$. In summary, in the process of MT, $\xi_{\Omega}(x)$ is formulated as

$$\xi_{\Omega}(x)=0,\ \text{when}\ F_{\Omega}<0, \tag{21a}$$

$$\xi_{\Omega}(x)=\frac{F_{\Omega}}{A_{\Omega}}\left[1-\frac{\cosh\sqrt{\frac{A_{\Omega}}{B_{\Omega}}}x}{\cosh\left(\sqrt{\frac{A_{\Omega}}{B_{\Omega}}}\frac{l_{\mathrm{g},\Omega}-t_{\mathrm{b}}}{2}\right)}\right], \tag{21b}$$

when $0\leqslant F_{\Omega}\leqslant F_{\mathrm{c},\Omega}$,

$$\xi_{\Omega}(x)=\begin{cases}\dfrac{F_{\Omega}}{A_{\Omega}}\left[1-\dfrac{\cosh\sqrt{\dfrac{A_{\Omega}}{B_{\Omega}}}x}{\cosh\left(\sqrt{\dfrac{A_{\Omega}}{B_{\Omega}}}\dfrac{l_{\mathrm{g},\Omega}-t_{\mathrm{b}}}{2}\right)}\right], \\ x\in\left[-\dfrac{l_{\mathrm{g},\Omega}-t_{\mathrm{b}}}{2},x_{1,\Omega}^{*}\right]\cup\left[x_{2,\Omega}^{*},\dfrac{l_{\mathrm{g},\Omega}-t_{\mathrm{b}}}{2}\right], \\ 1, \\ x\in\left[x_{1,\Omega}^{*},x_{2,\Omega}^{*}\right],\end{cases} \tag{21c}$$

when $F_{\Omega}>F_{\mathrm{c},\Omega}$.

The overall strains of the GI- type II GB mixture phase and the type I GB phase are defined as

$$\varepsilon_{\text{GI-GB},\Omega}=\frac{1}{l_{\mathrm{g},\Omega}-t_{\mathrm{b}}}\int_{-(l_{\mathrm{g},\Omega}-t_{\mathrm{b}})/2}^{(l_{\mathrm{g},\Omega}-t_{\mathrm{b}})/2}\varepsilon(x)\mathrm{d}x, \tag{22a}$$

$$\varepsilon_{\mathrm{GB_I},\Omega}=\frac{1}{t_{\mathrm{b}}}\left[\int_{-l_{\mathrm{g},\Omega}/2}^{-(l_{\mathrm{g},\Omega}-t_{\mathrm{b}})/2}\varepsilon(x)\mathrm{d}x+\int_{(l_{\mathrm{g},\Omega}-t_{\mathrm{b}})/2}^{l_{\mathrm{g},\Omega}/2}\varepsilon(x)\mathrm{d}x\right]. \tag{22b}$$

Moreover, the overall strain of the whole grain at the mesoscopic scale is defined as

$$\varepsilon_{\mathrm{G},\Omega}=\frac{l_{\mathrm{g},\Omega}-t_{\mathrm{b}}}{l_{\mathrm{g},\Omega}}\varepsilon_{\text{GI-GB},\Omega}+\frac{t_{\mathrm{b}}}{l_{\mathrm{g},\Omega}}\varepsilon_{\mathrm{GB_I},\Omega}. \tag{23}$$

As mentioned above, only the elastic deformation of GB phase is considered in this work. Without energy dissipation, the stress-strain relationship of the type I GB phase can be directly obtained by the Helmholtz free energy (Eq. (1a))

$$\sigma_{\Omega}=\frac{\partial\psi_{\mathrm{GB_I},\Omega}}{\partial\varepsilon_{\Omega}(x)}=E_{\mathrm{GB}}\varepsilon_{\Omega}(x),\quad x\in\left[-\frac{l_{\mathrm{g},\Omega}}{2},-\frac{l_{\mathrm{g},\Omega}-t_{\mathrm{b}}}{2}\right]\cup\left[\frac{l_{\mathrm{g},\Omega}-t_{\mathrm{b}}}{2},\frac{l_{\mathrm{g},\Omega}}{2}\right]. \tag{24}$$

It is noted that since σ_{Ω} is uniformly distributed, the strain field in the type I GB phase does not depend on the location x. Substituting Eqs. (12), (21), (22) and (24) into Eq. (23), it yields

$$\varepsilon_{\mathrm{G},\Omega}=\varepsilon_{\mathrm{G},\Omega}^{\mathrm{e}}+\varepsilon_{\mathrm{G},\Omega}^{\mathrm{tr}}, \tag{25a}$$

$$\varepsilon_{\mathrm{G},\Omega}^{\mathrm{e}}=\frac{l_{\mathrm{g},\Omega}-t_{\mathrm{b}}}{l_{\mathrm{g},\Omega}}\frac{\sigma_{\Omega}}{E_{\text{GI-GB},\Omega}}+\frac{t_{\mathrm{b}}}{l_{\mathrm{g},\Omega}}\frac{\sigma_{\Omega}}{E_{\mathrm{GB}}}, \tag{25b}$$

$$\varepsilon_{\mathrm{G},\Omega}^{\mathrm{tr}}=0, \quad \text{when } F_{\Omega}<0,$$

$$\varepsilon_{\mathrm{G},\Omega}^{\mathrm{tr}}=\frac{F_{\Omega}}{A_{\Omega}l_{\mathrm{g},\Omega}}\left[\left(l_{\mathrm{g},\Omega}-t_{\mathrm{b}}\right)-2\sqrt{\frac{B_{\Omega}}{A_{\Omega}}}\frac{\sinh\left(\sqrt{\dfrac{A_{\Omega}}{B_{\Omega}}}\dfrac{l_{\mathrm{g},\Omega}-t_{\mathrm{b}}}{2}\right)}{\cosh\left(\sqrt{\dfrac{A}{B}}\dfrac{l_{\mathrm{g}}-t_{\mathrm{b}}}{2}\right)}\right], \quad \text{when } 0\leqslant F_{\Omega}\leqslant F_{\mathrm{c},\Omega}, \tag{25c}$$

$$\varepsilon_{\mathrm{G},\Omega}^{\mathrm{tr}}=\frac{2F_{\Omega}}{A_{\Omega}l_{\mathrm{g},\Omega}}\left[\frac{1}{2}\left(l_{\mathrm{g},\Omega}-t_{\mathrm{b}}\right)-x_{2,\Omega}^{*}-\sqrt{\frac{B_{\Omega}}{A_{\Omega}}}\frac{\sinh\left(\sqrt{\dfrac{A_{\Omega}}{B_{\Omega}}}\dfrac{l_{\mathrm{g},\Omega}-t_{\mathrm{b}}}{2}\right)-\sinh\left(\sqrt{\dfrac{A_{\Omega}}{B_{\Omega}}}x_{2,\Omega}^{*}\right)}{\cosh\left(\sqrt{\dfrac{A_{\Omega}}{B_{\Omega}}}\dfrac{l_{\mathrm{g},\Omega}-t_{\mathrm{b}}}{2}\right)}\right]+\frac{2x_{2,\Omega}^{*}}{l_{\mathrm{g},\Omega}}, \quad \text{when } F_{\Omega}>F_{\mathrm{c},\Omega}.$$

Equation (25) gives the analytical expression for the overall strain of the whole grain $\varepsilon_{\mathrm{G},\Omega}$ at the mesoscopic scale. It should be pointed out that $\varepsilon_{\mathrm{G},\Omega}$ also represents the local strain of the Ω-th sub-domain at the macroscopic scale. The overall stress and strain of the specimen at the macroscopic scale can be obtained by the following volume average relationship

$$\Sigma=\frac{1}{N}\sum_{\Omega=1}^{N}\sigma_{\Omega}, \tag{26a}$$

$$E=\frac{1}{N}\sum_{\Omega=1}^{N}\varepsilon_{\mathrm{G},\Omega}. \tag{26b}$$

According to the geometric feature of the specimen, it is assumed that the local stresses in sub-domains are identical, i.e., $\sigma_1=\sigma_2=,...,\sigma_N$. In this case, according to Eq. (26a), we have

$$\sigma_{\Omega}=\Sigma. \tag{27}$$

Equation (27) is the scale transition rule from mesoscopic to macroscopic scale. Combining Eqs. (25), (26b) and (27), the analytical expression for overall strain of the specimen can be obtained

$$E=\frac{1}{N}\sum_{\Omega=1}^{N}\left(\frac{l_{\mathrm{g},\Omega}-t_{\mathrm{b}}}{l_{\mathrm{g},\Omega}}\frac{\Sigma}{E_{\text{GI-GB},\Omega}}+\frac{t_{\mathrm{b}}}{l_{\mathrm{g},\Omega}}\frac{\Sigma}{E_{\mathrm{GB}}}+\varepsilon_{\mathrm{G},\Omega}^{\mathrm{tr}}\right). \tag{28}$$

So far, the multiscale analytical model has been constructed. In the subsequent calculations, for a given applied stress Σ at the macroscopic scale, we can respectively use Eqs. (25) and (28) to get the local strain in the Ω-th sub-domain and overall strain of the specimen.

3. Model validation and discussion

The proposed model is verified by comparing the predicted results with the corresponding experimental data of Chen et al. [32]. In Chen et al. [32], the superelastic deformation for three types of NiTi SMA specimens are investigated, including the coarse-grained (GS = 235 nm), nano-grained (GS = 10 nm) and gradient nano-grained specimens. The gauge length of the specimens is 18 mm, and the loading rate is set as 1×10^{-4}/s. The GSs in the coarse-grained and nano-grained specimens are uniformed distributed. For the gradient nano-grained specimen, the GS changes from 10 nm at one end to 180 nm at the other end, and the GS at the central point of the specimen is 60 nm. Thus, in simulations, a quadratic function $l_g(X) = a(X/l)^2 + b(X/l) + c$ (a = 140 nm, b = −310 nm, c = 180 nm) is employed to describe the GS distribution along the axial direction. The material parameters used in the following simulations are E_{GI} = 60 GPa, E_{GB} = 50 GPa, g^{tr} = 0.0425, $\Delta s_{GI}^{\theta_0}(\theta - \theta_0)$ = 11.1 MPa, Y = 4.0 MPa, $S_0 l_e^2 = 6.0 \times 10^{-10}$ Pa m^2. The thickness of GB is set as 2 nm by referring to the existing literature [67]. The details for the determination of material parameters are provided in the Appendix A.

Figure 2(a) and (b) shows the experimental and predicted stress-strain responses of the coarse-grained (235 nm) and nano-grained (10 nm) NiTi SMA specimens. Figure 2(c)-(f) shows the predicted results of NiTi SMA with other typical

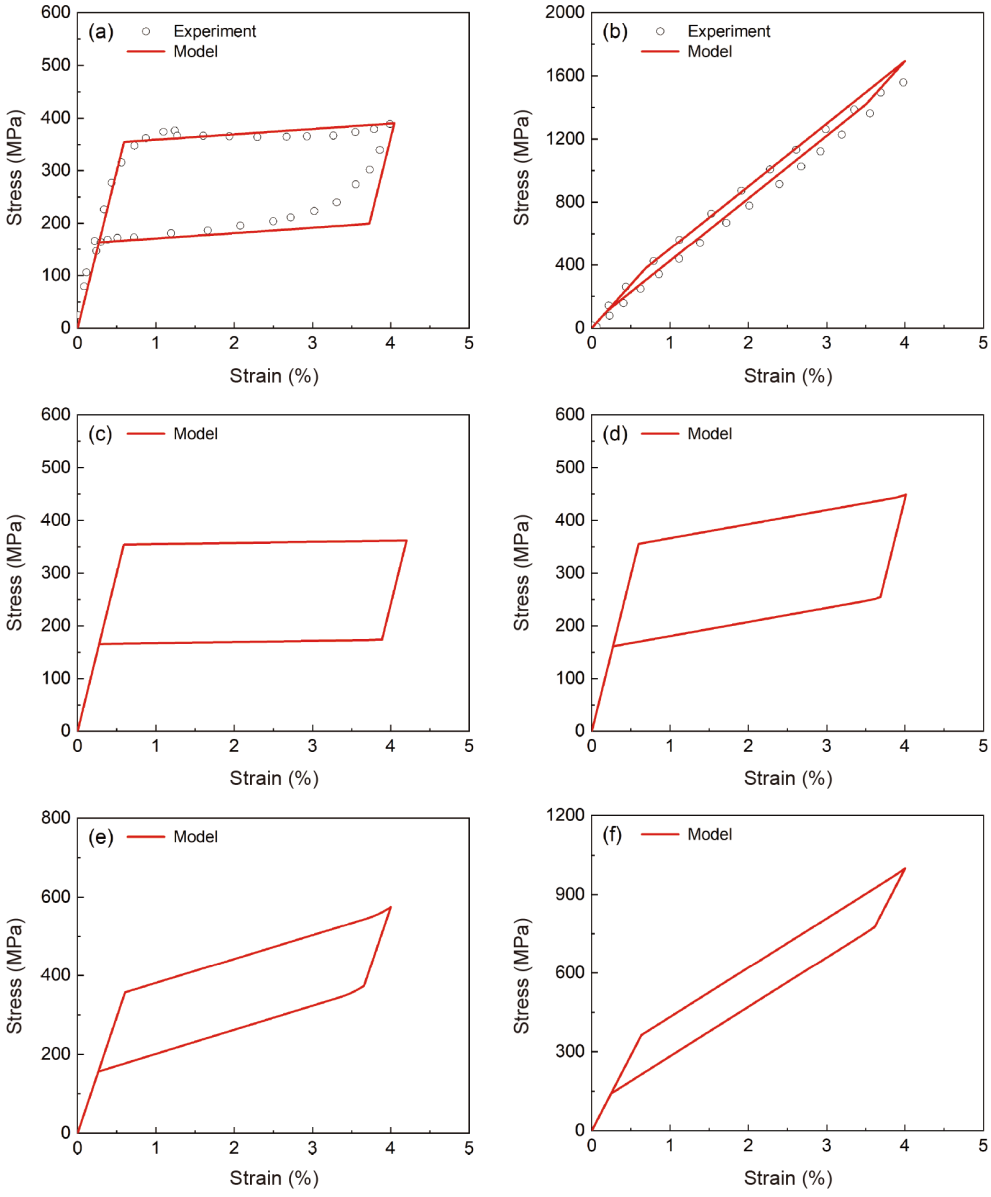

Figure 2 Superelastic deformation of NiTi SMAs with different GSs (the GSs are uniformly distributed). (a) GS = 235 nm; (b) GS = 10 nm; (c) GS = 1000 nm; (d) GS = 100 nm; (e) GS = 50 nm; (f) GS = 20 nm (The experimental data are cited from Ref. [32]).

GSs (1000, 200, 50 and 20 nm). It is seen that the superelastic deformation of NiTi SMAs depends on the GS strongly, i.e., for the coarse-grained specimen, the stress-strain response exhibits transformation plateau and large hysteresis loop. However, the transformation hardening modulus/hysteresis loop increases/decreases monotonically with decreasing GS. When the GS decreases to 10 nm, a quasi-linear response with very small hysteresis loop can be observed. These phenomena were also observed in some other experiments [16,20] and were well captured by the proposed model since (1) the increased volume fraction of GB phase with decreasing the GS was reflected and (2) the hindering effect of GB phase on the MT in GI phase has been reasonably considered. Figure 3(a) shows the overall stress-strain response of the gradient nano-grained specimen. Figure 3(b) gives the strain distribution along the axial direction when the overall strain reaches 3%. It is seen that the stress-strain response of the gradient nano-grained specimen exhibits high nonlinearity. Meanwhile, the strain field in the specimen is inhomogeneous, i.e., the strain in the region with large GS is much larger than that with small GS. Comparing the predicted results with the experimental data, it can be concluded that both the overall and local deformations of the gradient nano-grained specimen are reasonably captured by the proposed model.

The influence of the distribution form for the GS on the superelastic deformation of gradient nano-grained NiTi SMAs is further predicted. Figure 4(a) shows the first five different distributions, i.e., the GSs at the two ends of the specimen are fixed (180 and 10 nm), and the distributions satisfy the quadratic function relations. Figure 5(a) shows the latter five different distributions, i.e., the GS at the right end of the specimen is fixed (10 nm), and the distributions satisfy the linear function relations. Figures 4(b) and 5(b) show the predicted overall stress-strain responses. Figures 4(c) and 5(c) show the predicted distributions of strain field when the overall strain reaches 3%. It is concluded that the superelastic deformation of gradient nano-grained NiTi SMAs can be tailored by changing the distribution form of GS, and the proposed model provides a theoretical tool to design the gradient nano-grained NiTi SMAs with desired mechanical property.

It should be pointed out that in this work, we only focus on the isothermal superelastic deformation of gradient nano-grained NiTi SMAs in one loading-unloading cycle. The shape memory effect, superelasticity degradation during cyclic deformation, and the rate-dependent deformation originated from the thermo-mechanical coupling effect are also important phenomena observed in NiTi SMAs. A more comprehensive constitutive model is needed to describe these phenomena in gradient nano-grained NiTi SMAs, and this will be done in our future work.

4. Conclusion

(1) Based on the nonlocal continuum theory, a multiscale analytical model is proposed to describe the superelastic deformation of gradient nano-grained NiTi SMAs. The proposed model is first constructed at the mesoscopic scale by addressing the hindering effect of GB on the MT in GI phase, and then transited to the macroscopic scale by employing a scale transition rule. The main advantages of the proposed model are its analytical form and low computational cost.

(2) For the coarse-grained NiTi SMA specimen, the superelastic deformation exhibits transformation plateau and large hysteresis loop. In contrast, a quasi-linear response with a very small hysteresis loop can be observed for the nano-grained specimen. However, different from the coarse-grained and nano-grained NiTi SMAs, the stress-strain response of the gradient nano-grained specimen exhibits high nonlinearity. All these phenomena are well predicted by the proposed model since the underlying mechanisms for the GS-dependent deformation of NiTi SMA are reasonably captured.

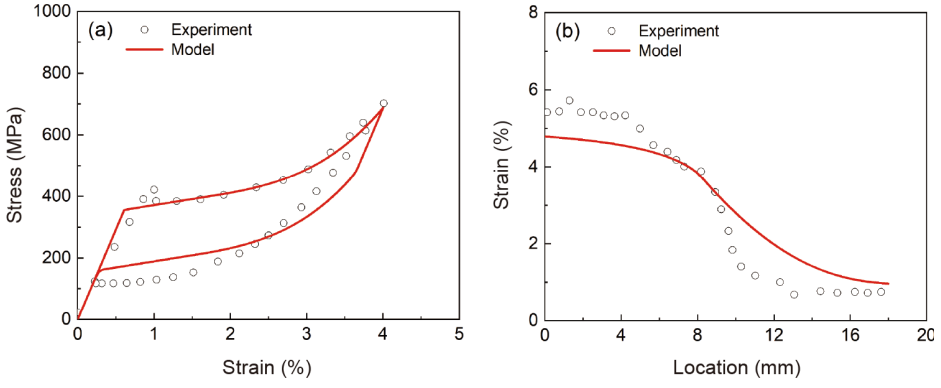

Figure 3 Superelastic deformation of gradient nano-grained NiTi SMAs (10-180 nm). (a) Stress-strain responses; (b) strain distribution along the axial direction (The experimental data are cited from Ref. [32]).

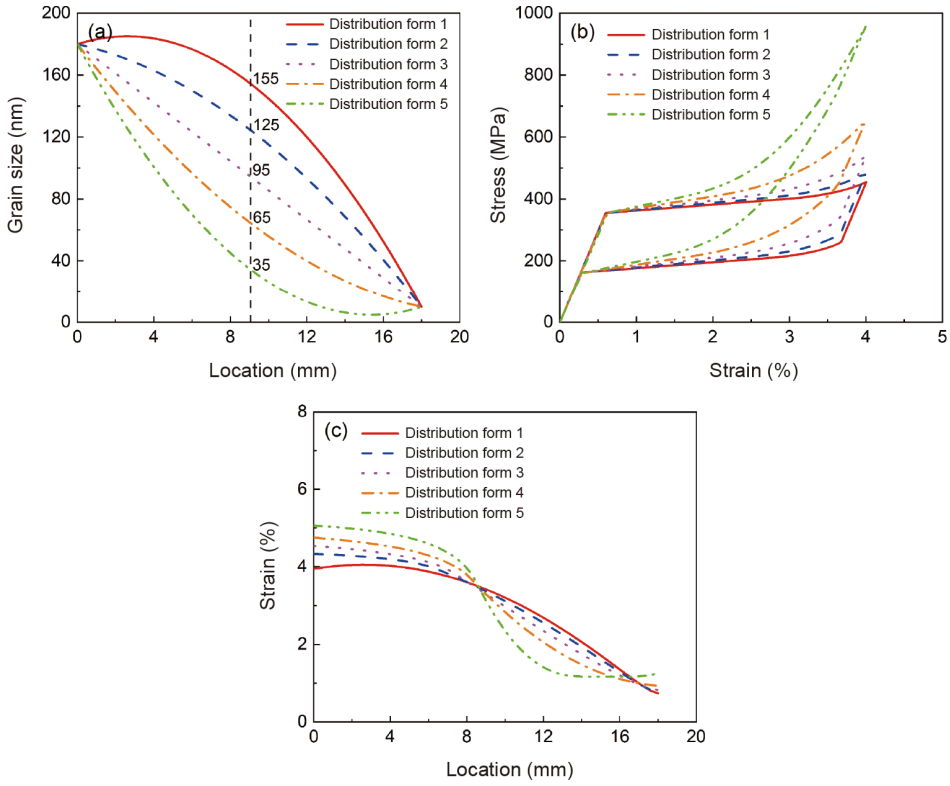

Figure 4 Influence of the GS distribution form on the superelastic deformation of gradient nano-grained NiTi SMAs. (a) The first five distributions of GS; (b) stress-strain responses; (c) strain distributions along the axial direction.

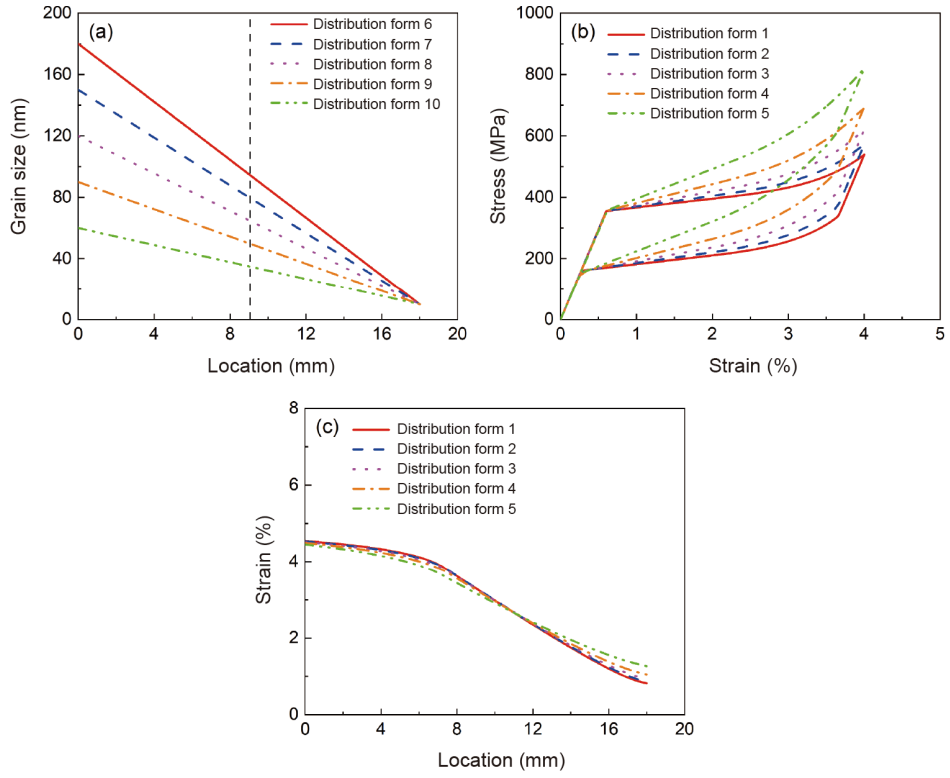

Figure 5 Influence of the GS distribution form on the superelastic deformation of gradient nano-grained NiTi SMAs. (a) The latter five distributions of GS; (b) stress-strain responses; (c) strain distributions along the axial direction.

(3) The influence of the distribution form for the GS on the deformation of gradient nano-grained NiTi SMAs is further predicted by the proposed. It is concluded that the superelasticity can be tailored by changing the distribution form of GS. The proposed model provides a theoretical tool to design this type of materials.

Appendix A

The material parameters used in the proposed model can be determined from the stress-strain curves of NiTi SMA specimens with two different grain sizes. For instance, the elastic modulus of GI phase can be obtained from the linear stress-strain response of NiTi SMA specimen with a GS of 235 nm at the beginning of deformation, as shown in Fig. 2 (a). Then, the elastic modulus of GB phase can be obtained by fitting the initial linear stress-strain response of the specimen with a GS of 10 nm, as shown in Fig. 2(b). The parameter g^{tr} controls the maximum transformation strain, and is set as 0.0425 by referring to Ahadi and Sun [12]. The parameter $\Delta s_{\mathrm{GI}}^{\theta_0}(\theta-\theta_0)$ controls the critical stress of MT. The parameter Y controls width of the hysteresis loop. These two parameters can be determined by fitting the start stress of forward and reverse MTs for the specimen with a GS of 235 nm, as shown in Fig. 2(a). The parameter $S_0 l_{\mathrm{e}}^2$ controls the additional transformation hardening effect caused by grain refinement, and can be determined by fitting the transformation hardening modulus of the specimen with a GS of 10 nm.

Conflict of interest *On behalf of all authors, the corresponding author states that there is no conflict of interest.*

Author contributions ***Bo Xu****: Conceptualization, Data curation, Formal analysis, Investigation, Methodology, Resources, Writing – Original draft.* ***Xingyu Zhou****: Software, Validation, Visualization, Writing – Review & Editing.* ***Chao Yu****: Conceptualization, Funding acquisition, Writing – Review & Editing.*

Acknowledgements *This work was supported by the National Natural Science Foundation of China (NSFC) (Grant Nos. 12072296, 12322203 and 12202294) and Sichuan Science and Technology Program (Grant No. 2024NSFSC1346) are greatly appreciated.*

1 J. M. Jani, M. Leary, A. Subic, and M. A. Gibson, A review of shape memory alloy research, applications and opportunities, Mater. Des. **56**, 1078 (2014).
2 H. Hou, E. Simsek, T. Ma, N. S. Johnson, S. Qian, C. Cissé, D. Stasak, N. Al Hasan, L. Zhou, Y. Hwang, R. Radermacher, V. I. Levitas, M. J. Kramer, M. A. Zaeem, A. P. Stebner, R. T. Ott, J. Cui, and I. Takeuchi, Fatigue-resistant high-performance elastocaloric materials made by additive manufacturing, Science **366**, 1116 (2019).
3 S. Qian, D. Catalini, J. Muehlbauer, B. Liu, H. Mevada, H. Hou, Y. Hwang, R. Radermacher, and I. Takeuchi, High-performance multi-mode elastocaloric cooling system, Science **380**, 722 (2023).
4 G. Zhou, Y. Zhu, S. Yao, and Q. Sun, Giant temperature span and cooling power in elastocaloric regenerator, Joule **7**, 2003 (2023).
5 M. Köhl, M. Bram, A. Moser, H. P. Buchkremer, T. Beck, and D. Stöver, Characterization of porous, net-shaped NiTi alloy regarding its damping and energy-absorbing capacity, Mater. Sci. Eng.-A **528**, 2454 (2011).
6 S. Saedi, E. Acar, H. Raji, S. E. Saghaian, and M. Mirsayar, Energy damping in shape memory alloys: A review, J. Alloys Compd. **956**, 170286 (2023).
7 B. S. Shariat, Q. Meng, A. S. Mahmud, Z. Wu, R. Bakhtiari, J. Zhang, F. Motazedian, H. Yang, G. Rio, T. Nam, and Y. Liu, Functionally graded shape memory alloys: Design, fabrication and experimental evaluation, Mater. Des. **124**, 225 (2017).
8 T. Odaira, S. Xu, X. Xu, T. Omori, and R. Kainuma, Elastocaloric switching effect induced by reentrant martensitic transformation, Appl. Phys. Rev. **7**, 031406 (2020).
9 P. Chen, Y. Liu, N. Min, M. Wang, X. Cai, M. Jin, and X. Jin, Enhanced two way shape memory effect in nanocrystalline NiTi shape memory alloy wires, Scr. Mater. **236**, 115669 (2023).
10 Z. Deng, K. Huang, H. Yin, and Q. Sun, Temperature-dependent mechanical properties and elastocaloric effects of multiphase nano-crystalline NiTi alloys, J. Alloy. Compd. **938**, 168547 (2023).
11 R. Delville, B. Malard, J. Pilch, P. Sittner, and D. Schryvers, Transmission electron microscopy investigation of dislocation slip during superelastic cycling of Ni-Ti wires, Int. J. Plast. **27**, 282 (2011).
12 A. Ahadi, and Q. Sun, Effects of grain size on the rate-dependent thermomechanical responses of nanostructured superelastic NiTi, Acta Mater. **76**, 186 (2014).
13 J. Chen, L. Xing, G. Fang, L. Lei, and W. Liu, Improved elastocaloric cooling performance in gradient-structured NiTi alloy processed by localized laser surface annealing, Acta Mater. **208**, 116741 (2021).
14 R. W. Armstrong, 60 years of Hall-Petch: Past to present nano-scale connections, Mater. Trans. **55**, 2 (2014).
15 E. N. Hahn, and M. A. Meyers, Grain-size dependent mechanical behavior of nanocrystalline metals, Mater. Sci. Eng.-A **646**, 101 (2015).
16 A. Ahadi, and Q. Sun, Stress hysteresis and temperature dependence of phase transition stress in nanostructured NiTi—Effects of grain size, Appl. Phys. Lett. **103**, 021902 (2013).
17 R. Delville, B. Malard, J. Pilch, P. Sittner, and D. Schryvers, Microstructure changes during non-conventional heat treatment of thin Ni-Ti wires by pulsed electric current studied by transmission electron microscopy, Acta Mater. **58**, 4503 (2010).
18 Y. Chen, O. Tyc, O. Molnárová, L. Heller, and P. Šittner, Tensile deformation of superelastic NiTi wires in wide temperature and microstructure ranges, Shap. Mem. Superelast. **5**, 42 (2019).
19 H. Lin, P. Hua, and Q. Sun, Effects of grain size and partial amorphization on elastocaloric cooling performance of nanostructured NiTi, Scr. Mater. **209**, 114371 (2022).
20 A. Ahadi, and Q. Sun, Stress-induced nanoscale phase transition in superelastic NiTi by *in situ* X-ray diffraction, Acta Mater. **90**, 272 (2015).
21 Q. P. Sun, A. Aslan, M. P. Li, and M. X. Chen, Effects of grain size on phase transition behavior of nanocrystalline shape memory alloys, Sci. China Tech. Sci. **57**, 671 (2014).
22 X. B. Shi, F. M. Guo, J. S. Zhang, H. L. Ding, and L. S. Cui, Grain size effect on stress hysteresis of nanocrystalline NiTi alloys, J. Alloy. Compd. **688**, 62 (2016).
23 Y. Chen, O. Tyc, L. Kadeřávek, O. Molnárová, L. Heller, and P. Šittner, Temperature and microstructure dependence of localized tensile deformation of superelastic NiTi wires, Mater. Des. **174**, 107797 (2019).
24 Z. Zhao, D. Jiang, Y. Xiao, J. Lin, and J. Min, Intrinsic response of nanocrystalline superelastic NiTi shape memory alloy, Extreme Mech. Lett. **60**, 101988 (2023).
25 P. Sedmák, P. Šittner, J. Pilch, and C. Curfs, Instability of cyclic superelastic deformation of NiTi investigated by synchrotron X-ray diffraction, Acta Mater. **94**, 257 (2015).
26 H. Chen, F. Xiao, X. Liang, Z. Li, Z. Li, X. Jin, N. Min, and T. Fukuda, Improvement of the stability of superelasticity and elastoca-

loric effect of a Ni-rich Ti-Ni alloy by precipitation and grain refinement, Scr. Mater. **162**, 230 (2019).
27 J. Chen, L. Lei, and G. Fang, Grain-size effects on the temperature-dependent elastocaloric cooling performance of polycrystalline NiTi alloy, J. Alloy. Compd. **927**, 166951 (2022).
28 P. Kabirifar, K. Chu, F. Ren, and Q. Sun, Effects of grain size on compressive behavior of NiTi polycrystalline superelastic macro- and micropillars, Mater. Lett. **214**, 53 (2018).
29 S. Ju, Y. Xiao, J. Lin, L. Gao, D. Chen, Z. Lu, C. Fang, and J. Min, Direct-current-assisted healing for functional degradation of nanocrystalline superelastic NiTi shape memory alloys, Metall. Mater. Trans. A **54**, 4625 (2023).
30 W. Ji, R. Zhou, P. Viveganantha, M. See Wu, H. Gao, and K. Zhou, Recent progress in gradient-structured metals and alloys, Prog. Mater. Sci. **140**, 101194 (2023).
31 K. Huang, Q. Sun, C. Yu, and H. Yin, Deformation behaviors of gradient nanostructured superelastic NiTi shape memory alloy, Mater. Sci. Eng.-A **786**, 139389 (2020).
32 J. Chen, Y. Wu, and H. Yin, *In situ* multi-field investigation of grain size effects on the rate-dependent thermomechanical responses of polycrystalline superelastic NiTi, Mater. Lett. **259**, 126845 (2020).
33 J. Chen, B. Liu, L. Xing, W. Liu, L. Lei, and G. Fang, Toward tunable mechanical behavior and enhanced elastocaloric effect in NiTi alloy by gradient structure, Acta Mater. **226**, 117609 (2022).
34 J. Chen, W. Wang, Q. Zhang, L. Lei, U. Ramamurty, and G. Fang, Temperature dependence of elastocaloric effect in a microstructurally graded NiTi alloy, Scr. Mater. **245**, 116060 (2024).
35 K. Yan, P. Wei, K. Chu, H. Wang, W. He, F. Ren, and Q. Sun, Fatigue-resistant heterogeneous gradient nanocrystalline NiTi shape memory alloy fabricated by pre-strain laser shock peening, Shap. Mem. Superelast. **8**, 107 (2022).
36 J. Chen, C. Zhao, S. Zhang, W. Zhang, W. Liu, L. Lei, U. Ramamurty, and G. Fang, Imparting high elastocaloric cooling potential to NiTi alloy by two-step enhancements, Mater. Sci. Eng.-A **892**, 146073 (2024).
37 D. C. Lagoudas, in: Shape Memory Alloys: Modeling and Engineering Applications (Springer, New York, 2008).
38 C. Cisse, W. Zaki, and T. Ben Zineb, A review of constitutive models and modeling techniques for shape memory alloys, Int. J. Plast. **76**, 244 (2016).
39 G. Z. Kang, C. Yu, and Q. H. Kan, in: Thermo-Mechanically Coupled Cyclic Deformation and Fatigue Failure of NiTi Shape Memory Alloys: Experiments, Simulations and Theories. (Springer, Singapore, 2023).
40 S. Dhala, S. Mishra, A. Tewari, and A. Alankar, Modeling of finite deformation of pseudoelastic NiTi shape memory alloy considering various inelasticity mechanisms, Int. J. Plast. **115**, 216 (2019).
41 Y. Xiao, and D. Jiang, Rate dependence of transformation pattern in superelastic NiTi tube, Extreme Mech. Lett. **39**, 100819 (2020).
42 X. Chang, K. Lavernhe-Taillard, and O. Hubert, Stochastic multiscale modeling of the thermomechanical behavior of polycrystalline shape memory alloys, Mech. Mater. **144**, 103361 (2020).
43 K. Kazinakis, S. Kyriakides, and C. M. Landis, Effect of tension/compression asymmetry and anisotropy on the response of pseudoelastic NiTi tubes under equibiaxial stress, Extreme Mech. Lett. **53**, 101689 (2022).
44 T. Zhou, C. Yu, G. Kang, Q. Kan, and D. Fang, A crystal plasticity based constitutive model accounting for R phase and two-step phase transition of polycrystalline NiTi shape memory alloys, Int. J. Solids Struct. **193-194**, 503 (2020).
45 L. Petrini, and A. Bertini, A three-dimensional phenomenological model describing cyclic behavior of shape memory alloys, Int. J. Plast. **125**, 348 (2020).
46 M. Rezaee-Hajidehi, K. Tůma, and S. Stupkiewicz, Gradient-enhanced thermomechanical 3D model for simulation of transformation patterns in pseudoelastic shape memory alloys, Int. J. Plast. **128**, 102589 (2020).
47 L. Xu, A. Solomou, T. Baxevanis, and D. Lagoudas, Finite strain constitutive modeling for shape memory alloys considering transformation-induced plasticity and two-way shape memory effect, Int. J. Solids Struct. **221**, 42 (2021).
48 M. A. Hossain, and T. Baxevanis, A finite strain thermomechanically-coupled constitutive model for phase transformation and (transformation-induced) plastic deformation in NiTi single crystals, Int. J. Plast. **139**, 102957 (2021).
49 M. Li, M. Chen, and Q. Sun, Nonlocal modeling and analysis of spatiotemporal patterns in non-isothermal phase transformation of NiTi strips, Int. J. Solids Struct. **221**, 103 (2021).
50 C. Yu, and G. Kang, A multiscale magneto-thermo-mechanically coupled model for ultra-low-field induced magneto-elastocaloric effect in magnetostrictive-shape memory alloy composite system, Int. J. Eng. Sci. **168**, 103539 (2021).
51 X. Ju, Z. Moumni, Y. Zhang, F. Zhang, J. Zhu, Z. Chen, and W. Zhang, A multi-physics, multi-scale and finite strain crystal plasticity-based model for pseudoelastic NiTi shape memory alloy, Int. J. Plast. **148**, 103146 (2022).
52 K. Kazinakis, S. Kyriakides, and C. M. Landis, Simulation of the response and evolution of localization in pseudoelastic NiTi tubes under biaxial stress states, Int. J. Plast. **151**, 103179 (2022).
53 C. Yu, G. Kang, Q. Sun, and D. Fang, Modeling the martensite reorientation and resulting zero/negative thermal expansion of shape memory alloys, J. Mech. Phys. Solids **127**, 295 (2019).
54 C. Yu, T. Zhou, Q. Kan, G. Kang, and D. Fang, A two-scale thermo-mechanically coupled model for anomalous martensite transformation and elastocaloric switching effect of shape memory alloy, J. Mech. Phys. Solids **164**, 104893 (2022).
55 C. Yu, H. M. Jiang, D. Song, Y. Zhu, and G. Kang, A multi-scale diffusional-mechanically coupled model for super-elastic NiTi shape memory alloy wires in hydrogen-rich environment, Int. J. Plast. **165**, 103614 (2023).
56 D. Song, C. Yu, C. Zhang, and G. Kang, Superelasticity degradation of NiTi shape memory alloy in wide ranges of temperature and loading level: Experimental observation and micromechanical constitutive model, Int. J. Plast. **161**, 103487 (2023).
57 Z. Rao, J. Leng, Z. Yan, L. Tan, and X. Yan, A three-dimensional constitutive model for shape memory alloy considering transformation-induced plasticity, two-way shape memory effect, plastic yield and tension-compression asymmetry, Eur. J. Mech.-A Solids **99**, 104945 (2023).
58 S. Tsimpoukis, and S. Kyriakides, Rate induced thermomechanical interactions in NiTi tensile tests on strips, J. Mech. Phys. Solids **184**, 105530 (2024).
59 Q. P. Sun, and Y. J. He, A multiscale continuum model of the grain-size dependence of the stress hysteresis in shape memory alloy polycrystals, Int. J. Solids Struct. **45**, 3868 (2008).
60 M. P. Li, and Q. P. Sun, Nanoscale phase transition behavior of shape memory alloys—Closed form solution of 1D effective modelling, J. Mech. Phys. Solids **110**, 21 (2018).
61 L. Qiao, and R. Radovitzky, Computational modeling of size-dependent superelasticity of shape memory alloys, J. Mech. Phys. Solids **93**, 93 (2016).
62 L. Qiao, J. J. Rimoli, Y. Chen, C. A. Schuh, and R. Radovitzky, Nonlocal superelastic model of size-dependent hardening and dissipation in single crystal Cu-Al-Ni shape memory alloys, Phys. Rev. Lett. **106**, 085504 (2011).
63 C. Yu, T. Zhou, D. Song, Q. Kan, and G. Kang, A two-scale thermo-mechanically coupled constitutive model for grain size- and rate-dependent deformation of nano-crystalline NiTi shape memory alloy, Int. J. Eng. Sci. **187**, 103843 (2023).
64 Q. Zhang, J. Chen, and G. Fang, From mechanical behavior and elastocaloric effect to microscopic mechanisms of gradient-structured NiTi alloy: A phase-field study, Int. J. Plast. **171**, 103809 (2023).
65 B. Xu, J. Xiong, C. Yu, C. Wang, Q. Wang, and G. Kang, Improved elastocaloric effect of NiTi shape memory alloys via microstructure

engineering: A phase field simulation, Int. J. Mech. Sci. **222**, 107256 (2022).
66 M. E. Gurtin, and L. Anand, A theory of strain-gradient plasticity for isotropic, plastically irrotational materials. Part I: Small deformations, J. Mech. Phys. Solids **53**, 1624 (2005).
67 R. Ahluwalia, S. S. Quek, and D. T. Wu, Simulation of grain size effects in nanocrystalline shape memory alloys, J. Appl. Phys. **117**, 244305 (2015).

梯度纳米晶NiTi形状记忆合金超弹性变形的多尺度解析模型

徐波, 周星宇, 于超

摘要 本文提出了一个描述梯度纳米晶NiTi形状记忆合金超弹性变形的多尺度非局部连续介质模型. 在细观尺度上, 将多晶体视为复合材料, 即将晶内相视为嵌在晶界相基体中的立方夹杂. 在晶内相的Helmholtz自由能中引入了内禀能量长度和梯度能. 基于虚功率原理和热力学第二定律, 导出了马氏体相变的判据. 强调了晶界相对晶内相中马氏体相变的阻碍作用. 通过推导模型的解析解并引入尺度过渡准则, 得到了梯度纳米晶试件宏观尺度下整体和局部的应力-应变响应. 通过与实验结果的对比, 验证了该模型的预测能力. 进一步预测和讨论了晶粒尺寸的分布形式对梯度纳米晶NiTi形状记忆合金超弹性变形的影响. 该模型的优点在于其解析形式和极高的计算效率, 为梯度纳米晶形状记忆合金的性能设计提供了理论工具.